Cobalt-molybdenum selenide double-shelled hollow nanocages derived from metal-organic frameworks as high performance electrodes for hybrid supercapacitor

Maryam Amiri,[a] Saied Saeed Hosseiny Davarani[a,*] Seyyed Ebrahim Moosavifard,[b,c] Yong-Qing Fu [d,*]

[a] *Faculty of Chemistry, Shahid Beheshti University, G.C., 1983963113, Evin, Tehran, Iran*

[b] *Department of Advanced Medical Sciences & Technologies, School of Medicine, Jahrom University of Medical Sciences, Jahrom 74148-46199, Iran*

[c] *Department of Biochemistry, School of Medicine, Jahrom University of Medical Sciences, Jahrom 74148-46199, Iran*

d Faculty of Engineering and Environment, University of Northumbria, Newcastle upon Tyne NE1 8ST, UK

* Corresponding authors: Prof. Saied Saeed Hosseiny Davarani, e-mail: ss-hosseiny@sbu.ac.ir; Prof. Richard Yongqing Fu, e-amil: Richard.fu@northumbria.ac.uk

Abstract

In this paper, we developed a sequential chemical etching and selenization processes to synthesize Co-MoSex double-shelled hollow nanocages (CMS-DSHNCs) as high performance electrode materials for supercapacitor applications. Co-MoO_x yolk-shelled hollow nanocages were firstly synthesized using a solvothermal process through facile ion-exchange reactions between zeolitic imidazolate framework-67 (ZIF-67) and MoO_4^{2-} ions. By applying a solvothermal temperature of 160 ^oC in the presence of SeO_3^{2-} and subsequently annealing strategy, CMS-DSHNCs were successfully synthesized with a yolk-shell hierarchically hollow and porous morphology of mixed metal selenides. The CMS-DSHNCs exhibit superior electrochemical properties as electrode materials for supercapacitor: e.g., a specific capacity of 1029.8 C g^{-1} at 2 A g^{-1} (3.089 C cm^{-2} at 6 mA cm^{-2}), a rate capability of ~76.14%, a capacity retention at 50 A g^{-1}, and a good cycle stability (95.2% capacity retention over 8000 cycles). A hybrid supercapacitor was constructed using the

CMS-DSHNCs as the cathode and activated carbon (AC) as the anode in a solution of 3 M KOH, and achieved a high specific energy of 45 Wh kg^{-1}, and a specific power up to 2222 W kg^{-1} with a good cycling stability of 94% after 8000 cycles.

Keywords: Capacitive-type electrode, double-shelled and hollow nanocages, Co-$MoSe_x$, asymmetric supercapacitor.

Introduction

Renewable and sustainable energy technologies are of prominent importance to cope with the overwhelming global environment changes and energy crisis. [1-3] Development of innovative energy storage technologies and identification of renewable and efficient energy resources are crucial to alleviate the huge energy demands worldwide.[4-6] Supercapacitors (SCs) have been regarded as one of the most desirable candidates for next-generation energy storage systems owing to their high power density, long cycle life, fast charge/discharge rates, and good durability.[7-9] Nevertheless, the practical applications of SCs are limited due to their unfavorable energy densities, even though they could achieve high power densities.[10-14] Hence, it is crucial to increase their energy densities without reducing their power densities through various methods, such as expanding the voltage window and boosting the specific capacities using various high performance electrodes. [15, 16]

Recently, transition metal dichalcogenides (TMDs) have received notable considerations as new types of Faradaic capacitive-type electrode materials owing to their superior properties, such as multiple oxidation states, metallic-like conductivities, sheet-like architectures, and broad-range cell potentials. [17, 18] Some of these TMDs, including $MoSe_2$, $Co_{0.85}Se$, $MnSe_2$, MoS_2/NiS and NiS_2 with their unique 2D nanostructures, have been considered as favorable materials for the SCs. [19-22] In particular, $MoSe_2$ possesses graphene-like nanosheet structures with narrow bandgaps, and the Mo ions cause the changes of oxidation states from +2 to +6, thus providing extra pseudo-capacitance abilities. [23-25]

Besides their chemical compositions, electrochemical performance of the SCs is also dependent upon nanostructures and morphologies of the electrode materials. [26-29] Recently, numerous efforts have been devoted to derive advanced electrode materials with controlled compositions/architectures using new design strategies such as metal-organic frameworks (MOFs) as precursors. [30, 31] MOFs have many good characteristics such as tailored morphology, hollow features, and facile transformation characteristics. They have been broadly applied as precursors of diverse nanostructured materials for energy storage applications, which may be impractical to achieve using the other methods. [32, 33] To this end, ZIF-67 (one of the typical Co-based MOFs) was employed as both sacrificial template and metal precursor in constructing well-defined hollow structures. [34-36] For example, $CoNi_2S_4$ nanocages, ZIF-67@Co-Ni LDH phosphate nanocages, carbon nanotubes/ZIF-67 CoS nanocages, nanoporous Co_3O_4 hollow polyhedrons, have been produced by using ZIF-67 as templates or precursors. [29, 37-39]

Nevertheless, these reported ZIF-67-derived materials have relatively simple configurations and microstructures.[35, 40, 41] Electrode materials with their hierarchically designed porous nanostructures can have more active interfacial sites and offer superior durability. As it is well-known [42-44], ion-exchange is one of the efficient approaches for transforming different compositions and structures of nanomaterials. Due to the inherent chemical instability of many MOFs, it is highly possible to control the conversion of simple MOFs into complex MOF-derived nanomaterials (including both of their chemical compositions and architectures) via ion-exchange reactions. [37, 45, 46] Furthermore, hollow structures with complex shapes, including multi-shell or yolk-shell structures, have recently received tremendous consideration for energy-related applications [47, 48] Particularly, multi-shelled hollow nanostructures can afford more contact areas of electrode/electrolyte, shorter charge transport channels, and more exposed active species, if compared with those of the conventionally hollow nanostructures, and thus they can result in fast Faradic redox reactions during electrochemical processes. [49-51] Additionally, the structural robustness of electrodes can be improved due to the interconnection of shells, which can achieve a longer life-span of the electrodes compared to the conventional yolk-shell and single-shelled counterparts. [52, 53] Therefore, we believe that a ZIF-67-derived system with multi-shelled structures and tailored molybdenum selenide compositions are highly profitable for the electrode

materials of SCs. Despite the advances in this field, there are few facile synthesis strategies and techniques for MOF-derived hybrid multi-shelled hollow architectures.

Motivated by the above new ideas, herein, we developed a facile MOF-assisted approach to construct Co-$MoSe_x$ double-shelled hollow nanocages (CMS-DSHNCs) for supercapacitor applications. Figure 1 exhibits the schematic design and preparation processes of the CMS-DSHNCs. In the first step, the ZIF-67 structure, used as a Co resource and a self-sacrifice template, is transformed into Co-MoO_x via an ion-exchange reaction between ZIF-67 nano-polyhedron and MoO_4^{2-} ions. A yolk-shell structure can then be formed using an anion-exchange process (Figure 1), during which MoO_4^{2-} ions are produced from ammonium heptamolybdate and then replace the 2-methylimidazole anions, thus forming the $CoMoO_x$ shell. Concurrently, the consistent consumption of the ZIF-67 core leads to a space between the remaining core and the newly formed $CoMoO_x$ shell. The H^+ ions originated from the hydrolysis process will continuously etch the ZIF-67 to release Co ions, which are then diffused outward and co-precipitated with Mo ions, thus forming hollow structures within the $CoMoO_x$ shell structures. [42, 54-56] At this stage, the outer shell is quite rough, and the inner shell has a hollow structure due to the reactions of MoO_4^{2-} and Co^{2+}, which can afford more active sites and reduce the charge transfer pathways (see Fig. 1). By heating up the thermal solvent in the presence of SeO_3^{2-}, the Co-MoO_x can be transformed into $CoMoSe_x$ DSHNCs, in which the SeO_3^{2-} ions are reduced to Se^{2-} and Mo^{6+} in MoO_4^{2-} is transformed into Mo^{4+} (stage Ⅲ) (Fig. 1). Crystallinity of Co-$MoSe_x$ can be enhanced after the high temperature post-annealing and crystalline phases (e.g., $CoSe_2$ and $MoSe_2$) are formed. The outer shell of the Co-$MoSe_x$ crystals comprises numerous pores and nanoparticles. Benefiting from their well-defined double-shelled porous structures, multiple elemental compositions, and significantly increased surface areas, the designed CMS-DSHNCs could achieve a much larger storage capacity with a rate capability comparable to those of the Co-MoO_x yolk-shelled hollow nanocages (CMO-YSHNCs).

EXPERIMENTAL

Materials and Synthesis

All chemicals used in this study were purchased from Sigma-Aldrich and Merck corporations. These include cobalt nitrate hexahydrate ($Co(NO_3)_2 \cdot 6H_2O$), sodium selenite (Na_2SeO_3), hydrazine monohydrate ammonium heptamolybdate tetrahydrate ($(NH_4)_6Mo_7O_{24}$), ethanol (C_2H_5OH), 2 methylimidazole($C_4H_6N_2$) and potassium hydroxide (KOH). The bare nickel foam substrate was purchased from LATECH (Singapore).

Figure 1 illustrates the fabrication procedures of CMO-YSHNCs. The ZIF-67 sample was first synthesized using a facile precipitation method at room temperature and then used as the precursor. Using a hydrothermal reaction, the ZIF-67 structure was transformed into Co-MoO_x via an ion-exchange reaction between ZIF-67 nano-polyhedron and MoO_4^{2-} ions (Figure 1). A yolk-shell structure was then formed using an anion-exchange process. By heating up the thermal solvent in the presence of SeO_3^{2-}, the Co-MoO_x can be transformed into $CoMoSe_x$ DSHNCs, in which the SeO_3^{2-} ions are reduced to Se^{2-} and Mo^{6+} in MoO_4^{2-} is transformed into Mo^{4+}. Crystallinity of Co-$MoSe_x$ can be enhanced using a high temperature post-annealing (Figure 1).

Synthesis of ZIF-67. ZIF-67 particles were produced based on a method reported in Ref. [57]. Components of 2-methylimidazole (16.0 mmol) and $Co(NO_3)_2 \cdot 6H_2O$ (8.00 mmol) were poured into two separated bottles with 200 mL of methanol under stirring for 10 min, which produced a pink and a transparent solutions, respectively. Afterwards, the pink solution was poured into the transparent solution under stirring for about 20 min, and then aged for 12 hrs. The collected purple precipitate was washed three times with absolute ethanol, followed by being dried at 60 °C under a vacuum for 12 h.

Synthesis of $CoMoSe_x$ DSHNCs. The synthesized ZIF-67 (100 mg) and $NaSeO_3$ (200 mg) were dissolved into 50 mL of ethanol. Ammonium heptamolybdate ($(NH_4)_6Mo_7O_{24}$) (158 mg)) dispersed in 8 mL of deionized water was poured into the above prepared solution for about 5 min under magnetic stirring. $N_2H_4 \cdot H_2O$ (1 mL) was added inside under stirring for about 20 min to obtain a homogeneous solution, which was heated at 60 °C for 1 h and then 160 °C for 6 h in a sealed Teflon autoclave. After centrifugated at 5000 rpm for 4 min with ethanol and dried at 60 °C for overnight, the obtained $CoMoSe_x$ DSHNCs were collected and then annealed at 300 °C for 2 h in N_2.

Synthesis of $CoMoO_x$. The synthesized ZIF-67 (100 mg) was dissolved into 50 mL of ethanol. Subsequently, 158 mg of ammonium heptamolybdate, dispersed in 8 mL of deionized water, was mixed into the above solution for 10 min under magnetic stirring. Afterwards, $N_2H_4 \cdot H_2O$ (1 mL) was added inside under continuous stirring for 20 min. Then the solution was heated at 60 °C for 1 h in a sealed Teflon autoclave. The obtained CMO-YSHNCs were collected by centrifugating at 5000 rpm for 4 min, washed with water and dried at 70 °C for 24 hrs. Eventually, the CMO-YSHNCs were annealed at 300 °C for 2 h in N_2.

Material characterization

To characterize electron states of the Co-$MoSe_x$ DSHNCs, X-ray photoelectron spectroscope (XPS, VG ESCALAB 250Xi MKII) with a Mg Ka X-ray source was used. Crystalline structures of the prepared materials were investigated using X-ray diffraction (XRD, Philip X'Pert) method with Cu Ka radiation. Morphology of the materials was characterized using a transmission electron microscope (TEM, Philips CM200) and a field-emission scanning electron microscope (FESEM: TESCAN Mira IIILMU), attached with an energy dispersive X-ray spectrometer (EDX). Pore size distribution, specific surface area, and total pore volume of the electrode materials were measured from N_2 adsorption-desorption experiments utilizing a Micromeritics ASAP-2010 instrument (at 77 K) by the Brunauer–Emmett–Teller (BET) method.

Electrochemical characterization

Electrochemical tests of the as-fabricated electrodes were performed employing a typical three-electrode cell, in which an Ag/AgCl and a Pt electrode were applied as the reference electrode and the counter electrode, respectively. The working electrode was made through pasting a mixture of as-fabricated nanocomposite, polyvinyl alcohol (PVA) and acetylene black, with their weight ratio of 85:10:5 in N-methyl pyrrolidone (NMP), onto a nickel foam (NF) electrode. The mass weight of the material was ~4 $mg \cdot cm^{-2}$ for each electrode. According to the charge-discharge (CD) curves, the specific electrode capacity, C_m, was measured from the formula (1) [58]:

$$C_m = \frac{I \times \Delta t}{m} \quad [C\ g^{-1}] \qquad (1)$$

where Δt is the discharge time (s), m is the total mass of electrode material (g), and I is the discharge current (A).

An asymmetric supercapacitor device of DSHNCs-CMS (+)//AC(-) was fabricated employing Co-$MoSe_x$ (positive electrode), activated carbon (AC, which is negative electrode), in 3 M KOH with a cellulosic paper (as a separator). To obtain a good performance of the asymmetric device, the mass ratio of the positive/negative electrode materials was optimized to be ~0.28. The total mass loading of the two electrodes was measured as 18 mg cm^{-2}, utilizing the following formula:

$$\frac{m_+}{m_-} = \frac{C_- * \Delta V_-}{C_+ * \Delta V_+} \quad (2)$$

In the above equation, m_+/m_- describes the mass ratio of two electroactive materials, and C_-/C_+ and $\Delta V_-/\Delta V_+$ display the ratios of capacitances and voltage range for the anode and cathode materials, respectively.

The specific power (P_s), specific energy (E_s), and specific capacitances (C_s) were then measured based on the Equations of (3) to (6), in which dt is the discharge time (s), v is the potential window (v), m is the total mass of active material (g), and I is the discharge current (A) of our devices.

$$E_{discharge} = I \int_{t_i}^{t_f} V.dt \quad (3)$$

$$E_{s,discharge} = \frac{E_{discharge}}{m_{el}\ 3.6} \quad (4)$$

$$C_s = \frac{2\ E_{s,discharge}}{V_{max}^2} \quad (5)$$

$$P_s = \frac{E_s}{\Delta t} \quad (6)$$

Results and discussion

Figure 2 shows the FESEM images, which reveal the morphological evolution of the as-prepared samples. As exhibited in Figs. 2a and 2b, the ZIF-67 nano-polyhedrons have a uniform size

distribution, dense structure, and smooth surface, which are consistent with those reports in literature [40, 59]. After reacted with MoO_4^{2-}, these ZIF-67 nano-polyhedrons are transformed into the Co-MoO_x YSHNCs (Figs. 2c-2e). These FESEM images of the as-prepared Co-MoOx YSHNCs reveal that the uniform nano-polyhedrons morphology can be well preserved, and the surface of Co-MoOx YSHNCs is much rougher, and significantly shrunk compared to that of ZIF-67, with many tiny particles grown on the shell. These significant changes of morphologies during the ion-exchange reactions are similar to those reported in Ref. [60, 61]. TEM images shown in Fig. 2f indicates that the Co-MoO_x YSHNCs have been converted into a hollow structure. Furthermore, the SEM and the elemental mapping images clearly show the uniform distributions of Co, Mo, and O elements throughout the Co-MoO_x YSHNCs (Fig. 2j) [46].

With the increase of solvothermal reaction temperature from 60 °C to 160 °C, the FESEM images shown in Figs. 3a and 3b show that the nanoscale polyhedron morphology of ZIF-67 is preserved. The surfaces of Co-$MoSe_x$ are rougher and coarser because the randomly distributed nanoparticles are adhered onto the surfaces of the polyhedrons when the Co-MoO_x reacts with Na_2SeO_3. During the selenization process, numerous agglomerated nanoparticles are produced on the surfaces of porous structures. The structure shrinks during the high temperature selenization process, thus forming numerous surface pores. Such a porous architecture can enhance ion-transport kinetics, generating high rate capability and capacity of the SCs.

TEM images of the Co-$MoSe_x$ sample (Figs. 3c and 3d) show the highly porous texture of the outer and inner shells with double-shelled hollow nanocages structures. Such unique structures with porous nature could provide abundant active sites and effective infiltration of electrolyte, thus enhancing the electrochemical properties of the Co-$MoSe_x$ samples. A magnified TEM image of the Co-$MoSe_x$ (Figs. 3c and 3d) shows that both its inner and outer shells possess a polyhedron shape [62, 63]. Porous nanoparticle-assembled hollow nanocages enhance the penetration of the electrolytes into both exterior and interior spaces of the hollow nanocages, and form effective ion diffusion pathways through increased electroactive areas. This structure can also effectively inhibit the aggregation of nanoparticles during the electrochemical reactions. SEM and the elemental mapping images (Figure 3e) display uniform distributions of Co, Mo, and Se elements throughout the nanocages-based Co-$MoSe_x$ double-shelled hollow nanocages.

Fig. 4a shows the crystalline phases of the prepared samples, obtained from XRD analysis. The main diffraction peaks of Co-$MoSe_x$ at 34.1°, 37.8°, 47.7°, 51.7°, and 56.8° are corresponding to the planes of cubic $CoSe_2$ (PDF No. 088-1712). The other peaks located at 13.6°, 31.4°, 34.4°, 37.8°, 47.4°, 55.8°, 57.8°, 56.9°, and 62.4° are assigned to the planes of hexagonal $MoSe_2$ (PDF No. 077-1715). The pattern of Co-MoO_x exhibits indistinct diffraction peaks with considerable noise, indicating its poor crystallinity. The visible peaks at 28.5°, 32.2°, 40.3°, 52.7°, and 61.2° are assigned to those of the $CoMoO_4$ (PDF No. 073-1331). Furthermore, no extra peaks of other phases in the XRD patterns of Co-$MoSe_x$ suggests the complete transformation from Co-MoO_x to Co-$MoSe_x$. The XRD pattern of the synthesized ZIF-67 is shown in Fig. SI, and the results are same with those of the ZIF-67 crystals reported in literature [38, 64, 65].

EDX spectrum of the Co-MoO_x (Fig. 4b) confirms the existence of Co, Mo, and O elements and their atomic percentages are 32.8%, 15.41%, and 51.79%, respectively. EDX spectrum of the Co-MoSex displays that the atomic percentages of Co, Mo, and Se elements are 26.4%, 21.5%, and 52.1%, respectively (Fig. 4c). Meanwhile, EDX spectra of ZIF-67 shown in Figure 3d reveal that the percentages of Co, C, N, and O atoms are 15.35%, 49.1%, 34.8%, and 0.7%, respectively (Fig. 4d).

For the XPS spectrum of Co 2p, the peaks at 793.1 eV (Co $2p_{1/2}$) and 778.1 eV (Co $2p_{3/2}$) are the characteristic peaks of Co^{2+}. The peaks located at 796 eV (Co $2p_{1/2}$ band) and 780.6 eV (Co $2p_{3/2}$ band) are assigned to those of the Co^{3+}[66]. The satellite peaks at 798.5 eV (Co $2p_{1/2}$ band) and 782.8 eV (Co $2p_{3/2}$ band) are assigned to those of the Co^{2+} [67, 68]. Results clearly show the coexistence of cobalt selenide, oxide, or hydroxide near the surface. For high-resolution Mo 3d spectrum (Fig. 2(d)), the two main peaks at 228 eV and 232 eV with a spin–orbit splitting energy of 3.3 eV are attributed to Mo 3d3/2 and 3d 5/2 of the Co-MoSex, respectively, and two other fitting peaks at 230.4 and 233.5 eV are assigned to those of Mo $3d_{5/2}$ and Mo $3d_{3/2}$ of Mo^{+5} [69, 70]. The Se 3d XPS spectrum represents the main peaks at 55 and 54 eV, which are the two orbital peaks of Se^{2-} $3d_{3/2}$ and Se^{2-} $3d_{5/2}$, respectively. This prove the presence of two oxidized chemical states for the Se element and the existence of Se^{2-} in the Co-$MoSe_x$. The extra peak situated at 59.1 eV is associated to the SeOx, which is the high oxide state of Se [71]. In addition, XPS analysis shows that Co-MoSex has lower binding energies for both Mo and Co than those of Co-Mo–Se and Cu-

Co-Sex hollow spheres reported in literature [72, 73], indicating the higher electron concentrations for the transition metals in the outer orbits of the MSex phase (Fig. 4e).

Surface areas of the prepared samples determined from N_2 adsorption-desorption isotherms are presented in Fig. 4f. The corresponding readings of Co-$MoSe_x$ and Co-MoO_x are estimated to be 98 $m^2\ g^{-1}$ and 64 $m^2\ g^{-1}$, respectively. The large surface areas of the Co-MoOx and Co-MoSex are associated to their porous structures with an increase in the number of active sites, which is useful for improving the electron transfer kinetics. Moreover, the porous nature of the Co-$MoSe_x$ sample provides effective channels for ions-electron transport kinetics. Clearly, Co-$MoSe_x$ has a larger surface area, which is beneficial for providing more electrolyte adsorption sites and shortened diffusion distances of charges. Besides, the pore distribution of prepared samples acquired by the BJH shows that Co-$MoSe_x$ and Co-MoO_x have a wide pore distribution in the mesoporous range. The large surface area of Co-$MoSe_x$ with a tailored mesoporous structure contribute to the enhanced electrochemical performance.

Electrochemical properties

Electrochemical performance of the electrodes was evaluated using a three-electrode cell through cyclic voltammetry (CV) and galvanostatic charge discharge (GCD) measurements in 3.0 M KOH. Fig. 5a shows the obtained CV curves of Ni foam, Zif-67, Co-$MoSe_x$ DSHNCs and CMO-YSHNCs tested at a constant scan rate of 50 mV s^{-1} in the wide potential range of -0.3 to ~0.7 V (vs. Ag/AgCl electrode).

The CV curves display a non-rectangular shape which demonstrates the Faradaic nature of the electrode materials and exhibits that the charge storage mechanism of $CoMoSe_x$ is due to the Faradaic redox reactions. The curve consists of 0.26 V and -0.06 V (reduction) and redox peaks at 0.36 V (oxidation). This shows that the reversible redox reaction between different valence states of Mo (i.e., exchange Mo^{3+} and Mo^{4+} and vice versa, and Co^{2+} and Co^{3+}) are overlapped with each other and connected with OH^- ions [70, 71, 74-76].

$$CoMoSe_x + 2OH^- \rightarrow MoSeOH + CoSeOH + 2e^- \quad (1)$$

$$CoSe_xOH + OH^- \rightarrow CoSe_xO + H_2O + e^- \quad (2)$$

$MoSe_2 + OH^- \rightarrow MoSe_2.2OH + 2e^-$ (3)

The higher redox peak and larger CV integral area of the CMS-DSHNCs electrode indicate their larger specific capacities and faster reaction kinetics in comparisons with those of the CMO-YSHNCs. This is due to a combination of double-shelled hollow structures, tailored cobalt-molybdenum selenide compositions, and the increased conductivity of the Co-$MoSe_x$. The CV curves of CMO-YSHNCs and CMS-DSHNCs electrodes at scan rates from 10 to 50 mV s^{-1} are presented in Figs. 5b and 5c. Both the areas of CV curves and current densities are continuously increased with the increase of the scan rate, indicating the reversible characteristics and superior capacitive behavior of the electrodes. Furthermore, the shapes of the curves do not show significant changes, and the redox peaks are slightly shifted to higher or lower potentials, even at higher scan rates. These indicate that the Co-$MoSe_x$ has rapid ionic and electronic transfer and rate capabilities. The high capacity values with a remarkable rate performance of the CMS-DSHNCs are associated with the hollow double-shell structure, which increases the surface area, magnifies the electrical conductivity, and increases the pseudo-capacitance of the CMS-DSHNCs electrode. For the Co-$MoSe_x$ structure, the hollow structure increases the surface areas and provides more electroactive sites, and the porous nanoparticles on the surface of the CMS-DSHNCs can increase both the electron and ion transportations.

To examine the charge storage kinetics, the calibration curves for the oxidative/reductive peak currents versus the square root of scan rate ($\upsilon^{1/2}$) were obtained, and the diffusion-controlled charge storage mechanism of the CMS-DSHNCs electrode can be obtained. We applied the equation of the power-law:

$$\log i_p = \log a + b \log(\upsilon) \quad (4)$$

where i_p represents the peak current, υ is the scan rates, a is a constant, and b is the power-law exponent. The value of b from the CV curves can be obtained from the slope of the linear fit of the curve of log (υ) versus log (i_p), as represented in Fig. 5e. When the b value is ~1, it means that the electrode shows a capacitive-type nature, whereas when the b value is 0.50, the behavior of the electrode is similar to that of the battery-type one. From the faradaic peak current values of CMS-DSHNCs electrode, the b values for the reductive and oxidative peaks are 0.888 and 0.874, respectively, which indicate that it has a capacitive-type behavior.

Fig. 5f shows the GCD curves of the Co-$MoSe_x$ and CMO-YSHNCs measured at a fixed current density of 2 Ag^{-1} with a potential range of -0.2 to 0.58 V (vs. Ag/AgCl). The nonlinear behaviors of the GCD curves at all the current densities demonstrate the faradaic redox reactions of this electrode material, which is in a good agreement with the CV curves. The GCD curves of the CMS-DSHNCs electrode at difference current densities from 2 to 50 Ag^{-1} are shown in Fig. 5g. For the CMS-DSHNCs electrode, the obtained specific capacities are 1029.8, 1002.2, 973.8, 900, 852.65, 830.1 and 784.1 C g^{-1} with the current densities of 2, 4, 8, 12, 16, 20 and 50 A g^{-1}, respectively. The CMS-DSHNCs electrode shows symmetric characteristics, demonstrating its reasonably good Coulombic efficiency. The CMO-YSHNCs electrodes exhibit the corresponding values of 809, 728.5, 620, 560.1, 522.3, 495.2 and 452.3 C g^{-1}, respectively, as represented in Fig. 5h. The above results suggest that the CMS-DSHNCs electrode shows higher specific capacities at the different current densities and excellent electrochemical performance.

The CMS-DSHNCs electrode has a specific capacity of 1029.8 C g^{-1} (3.84 C cm^{-2}) at 2 A g^{-1} which is higher than that of the CMO-YSHNCs electrode (809 C g^{-1} at 2 Ag^{-1}). By increasing the current density to 50 A g^{-1}, the CMS-DSHNCs electrode maintains 76.14% of its initial specific capacity at the 2 A g^{-1}, indicating its better rate capability than that of the CMO-YSHNCs electrode (with only 55.87 % as shown in Fig. 5i). The higher rate capability of the CMS-DSHNCs electrode is mainly attributed to its hierarchically porous structures of double-shelled architecture, in which the outer shell comprises numerous pores and nanoparticles. Such designed structures enable efficient pathways for fast diffusion of ions and expose more reactive sites for the faradaic reactions.

Cyclability is one of the critical requirements for high-performance SCs. The cycling performance of the CMS-DSHNCs and CMO-YSHNCs electrodes was evaluated by repeating charge-discharge cycles at a current density of 2 A g^{-1}, and the results are exhibited in Fig. 5j. About 4.8% and 9.6 % loss in specific capacities of the CMS-DSHNCs and CMO-YSHNCs electrodes were obtained after 8000 successive cycles for electrodes, indicating its good kinetic reversibility and superior cycling stability.

EIS was further performed to gain insights into electrical conductivity and reaction kinetics of the CMS-DSHNCs and CMO-YSHNCs electrodes, and the obtained results are shown in Fig. 5k. The Nyquist plots show a slightly lower internal resistance for the CMS-DSHNCs electrode (0.32 Ω) than that of the CMO-YSHNCs (0.41 Ω) electrode, demonstrating the lower interfacial contact

resistance and a lower electrolyte resistance of the CMS-DSHNCs. The lower R_{ct} of the CMS-DSHNCs electrode proves its faster electron transfer kinetics. In the low-frequency region, the appearance of a linear line with a much larger slope suggests a lower ion migration/diffusion resistance (Warburg) for the CMS-DSHNCs electrode. These results prove the superior electrochemical efficiency of the CMS-DSHNCs electrode, which is consistent with the GCD and CV results. To further check the long term performance of the Co-MoSex and Co-Mox electrodes, the EIS profiles were also plotted after the repeatability tests, and the results are shown in Fig. S2(A) (in the Supporting Information EI). There are no noticeable changes in the Rs and Rct values for the electrodes after 8000 cycles, suggesting a good stability of both the electrodes.

The good electrochemical efficiency of the CMS-DSHNCs electrode are attributed to the following reasons:

(1) The unique architecture of the CMS-DSHNCs reduce the charge-transfer resistance, and ensure a fast electron transport kinetics to the nickel foam substrate, thus intensifying the rate capability;

(2) The unique porous texture and numerous nanoparticles on the surface of the CMS-DSHNCs sample reduce the diffusion pathways for the ion/ electron transport and enhance the concentration of the active sites;

(3) The presence of selenium in the CMS-DSHNCs structure enhances its interior conductivity and structural stability.

Electrochemical performance of CMS-DSHNCs (+)//AC (-) device

To confirm the practical applications of the supercapacitors developed in this work, we manufactured a hybrid supercapacitor utilizing Co-$MoSe_x$ electrode as the positive electrode, and the activated carbon as the desired negative electrode. Fig. 5a shows the CV curves of the Co-$MoSe_x$ and AC electrodes at 30 mV s^{-1}. Figs. 5b and 5c illustrate the CV and GCD profiles measured at various scan rates and current densities for the assembled CMS-DSHNCs (+)//AC (-) device. The CV curves show a quasi-rectangular shape with a pair of broad redox peaks with minor deviations at high scan rates over the potential range 0 and 1.6 V. By increasing the potential window from 1 to 1.6 V, the capacity of the device is increased. As the result, the energy density has been increased

with increasing operating voltage. The overall CV curves display combined faradaic properties and electrical double-layer capacitive due to the contributions from Co-$MoSe_x$ and AC electrodes. The specific capacitances of the CMS-DSHNCs (+)//AC (-) asymmetric supercapacitor are 125, 111.2, 96, 80 and 78.6 Fg^{-1} at current densities of 1, 2, 4, 16 and 32 Ag^{-1}, respectively.

As can be seen in Fig. 6d, the device can maintain 62.8% of its initial capacitance after the current density is increased from 1 to 32 A g^{-1}. The Ragone plot shown in Fig. 6e demonstrates that the CMS-DSHNCs (+)//AC (-) device has an excellent performance compared to many results of similar devices reports in literature (see Table 1). It is worthwhile to mention that the CMS-DSHNCs (+)//AC (-) device still show an energy density of 45 Wh kg^{-1} at a high power density of 2222 W kg^{-1}. To manifest the practical performance of the Co-$MoSe_x$//AC device, two CMS-DSHNCs (+)//AC (-) devices are connected in series and then employed to successfully power a green light-emitting diode (LED) for more than 30 mins (see inset of Fig. 6e).

Fig. 6f displays the long-term cycling performance of the CMS-DSHNCs (+)//AC (-) device at a current density of 34 mA cm^{-2}. Results reveal that the CMS-DSHNCs (+)//AC (-) device maintains 94% of its initial capacitance after 8000 cycles, suggesting its superior cycling stability. Moreover, FE-SEM and TEM images of the cycling-tested electrodes were obtained to investigate any changes in the structure of CMS-DSHNC samples after 8000 cycles. The FE-SEM image (Fig. 6f inset) shows that nanoparticles can be observed on the surfaces of the nanocages, and the shapes of the double-shelled hollow nanocages have not been severely damaged, indicating the superior morphological durability of the CMS-DSHNCs sample. Meanwhile, the TEM image (Fig. 6f inset) shows that the morphology of CMS-DSHNCs after the durability test is similar to that before the durability test, and no notable aggregation among particles can be seen.

EIS analysis was further conducted to study the kinetic behaviors of two electrode systems. Fig. S2. shows the Nyquist plot of CMS-DSHNCs (+)//AC (-) device before and after 8000 cycle. The results from the EIS analysis show small values of Rct (1.2) and Rs (0.72), which prove that the CMS-DSHNCs maintain fast ion-electron transport kinetics throughout the whole redox process.

Conclusions

In summary, we have for the first time reported Co-$MoSe_x$ double-shelled hollow nanocages (CMS-DSHNCs) electrode by a facile and efficacious MOF-assisted strategy. Thanks to the desired morphological features of hierarchical hollow architectures, the synergistic effects of the components, and the significant role of the Se element, which leads to simplified ion/electron charge transfer and boosting reaction kinetics, the CMS-DSHNCs electrode delivered a desirable specific capacity of 1029.8 C g^{-1} at 2 A g^{-1} (3.089 C cm^{-2} at 6 mA cm^{-2}), a rate capability with 76.14% capacity retention at 50 A g^{-1}, and long-term stability with 94% of the initial capacity retained after 8000 cycles at 10 A g^{-1}. The ASC device constructed with the CMS-DSHNCs and AC electrodes delivered a high energy density of 45 Wh kg^{-1} at a power density of 2222 W kg^{-1} and prominent durability. Utilizing the reasonable energy/power densities, the as-fabricated CMS-DSHNCs (+)//AC (-) devices were utilized to power a red LED. Thus, in view of the enormous variation of MOFs with different compositions and morphologies, the method developed here may open up a novel and innovative approach to manipulating the structure of classical MOFs for splendid energy storage applications.

References

[1] L. Zhang, D. Shi, T. Liu, M. Jaroniec, J. Yu, Nickel-based materials for supercapacitors, Materials Today 25 (2019) 35-65.
[2] G. Zhou, L. Xu, G. Hu, L. Mai, Y. Cui, Nanowires for electrochemical energy storage, Chemical Reviews 119(20) (2019) 11042-11109.
[3] L. Jiang, Y. Lu, C. Zhao, L. Liu, J. Zhang, Q. Zhang, X. Shen, J. Zhao, X. Yu, H. Li, Building aqueous K-ion batteries for energy storage, Nature Energy 4(6) (2019) 495-503.
[4] B. Wang, T. Ruan, Y. Chen, F. Jin, L. Peng, Y. Zhou, D. Wang, S. Dou, Graphene-based composites for electrochemical energy storage, Energy Storage Materials 24 (2020) 22-51.
[5] S. Koohi-Fayegh, M. Rosen, A review of energy storage types, applications and recent developments, Journal of Energy Storage 27 (2020) 101047.
[6] A.M. Zardkhoshoui, S.S.H. Davarani, Ultra-high energy density supercapacitors based on metal–organic framework derived yolk–shell Cu–Co–P hollow nanospheres and CuFeS 2 nanosheet arrays, Dalton Transactions 49(10) (2020) 3353-3364.
[7] Q. Zhu, D. Zhao, M. Cheng, J. Zhou, K.A. Owusu, L. Mai, Y. Yu, A new view of supercapacitors: integrated supercapacitors, Advanced Energy Materials 9(36) (2019) 1901081.
[8] J. Yan, S. Li, B. Lan, Y. Wu, P.S. Lee, Rational design of nanostructured electrode materials toward multifunctional supercapacitors, Advanced Functional Materials 30(2) (2020) 1902564.
[9] Q. Jiang, N. Kurra, M. Alhabeb, Y. Gogotsi, H.N. Alshareef, All pseudocapacitive MXene‐RuO2 asymmetric supercapacitors, Advanced Energy Materials 8(13) (2018) 1703043.

[10] A. Eftekhari, The mechanism of ultrafast supercapacitors, Journal of Materials Chemistry A 6(7) (2018) 2866-2876.
[11] M. Salanne, B. Rotenberg, K. Naoi, K. Kaneko, P.-L. Taberna, C.P. Grey, B. Dunn, P. Simon, Efficient storage mechanisms for building better supercapacitors, Nature Energy 1(6) (2016) 1-10.
[12] M. Amiri, S.S.H. Davarani, S.K. Kaverlavani, S.E. Moosavifard, M. Shamsipur, Construction of Hierarchical Nanoporous $CuCo_2V_2O_8$ Hollow Spheres as a Novel Electrode Material for High-performance Asymmetric Supercapacitors, Applied Surface Science (2020) 146855.
[13] M. Amiri, S.E. Moosavifard, S.S.H. Davarani, S.K. Kaverlavani, M. Shamsipur, MnCoP hollow nanocubes as novel electrode material for asymmetric supercapacitors, Chemical Engineering Journal 420 (2021) 129910.
[14] M. Amiri, S.E. Moosavifard, S.S. Hosseiny Davarani, M. Shamsipur, Novel Rugby-Ball-like $FeCoCuS_2$ Triple-Shelled Hollow Nanostructures with Enhanced Performance for Supercapattery, Energy & Fuels (2021).
[15] P. Liu, J. Yan, Z. Guang, Y. Huang, X. Li, W. Huang, Recent advancements of polyaniline-based nanocomposites for supercapacitors, Journal of Power Sources 424 (2019) 108-130.
[16] L. Abbasi, M. Arvand, S.E. Moosavifard, Corrigendum to 'Facile template-free synthesis of 3D hierarchical ravine-like interconnected $MnCo_2S_4$ nanosheet arrays for hybrid energy storage device'[Carbon 161 (2020) 299–308], Carbon (2020).
[17] J. Cherusseri, N. Choudhary, K.S. Kumar, Y. Jung, J. Thomas, Recent trends in transition metal dichalcogenide based supercapacitor electrodes, Nanoscale Horizons 4(4) (2019) 840-858.
[18] J. Turley, S. Mukherjee, E. Mansfield, J.D. Holm, L. David, G. Singh, Exfoliated transition metal dichalcogenide (TMD) nanosheets for supercapacitor and sodium ion battery applications, 2019.
[19] X. Zhao, X. Li, Y. Zhao, Z. Su, R. Wang, Facile synthesis of Tremelliform Co0. 85Se nanosheets for supercapacitor, Journal of Alloys and Compounds 697 (2017) 124-131.
[20] M.S. Javed, S.S.A. Shah, S. Hussain, S. Tan, W. Mai, Mesoporous manganese-selenide microflowers with enhanced electrochemical performance as a flexible symmetric 1.8 V supercapacitor, Chemical Engineering Journal 382 (2020) 122814.
[21] Q. Qin, L. Chen, T. Wei, X. Liu, MoS_2/NiS yolk–shell microsphere ‐ based electrodes for overall water splitting and asymmetric supercapacitor, Small 15(29) (2019) 1803639.
[22] B. Guan, Y. Li, B. Yin, K. Liu, D. Wang, H. Zhang, C. Cheng, Synthesis of hierarchical NiS microflowers for high performance asymmetric supercapacitor, Chemical Engineering Journal 308 (2017) 1165-1173.
[23] S. Dutta, S. De, MoS_2 nanosheet/rGO hybrid: an electrode material for high performance thin film supercapacitor, Materials Today: Proceedings 5(3) (2018) 9771-9775.
[24] X. Liu, J.-Z. Zhang, K.-J. Huang, P. Hao, Net-like molybdenum selenide–acetylene black supported on Ni foam for high-performance supercapacitor electrodes and hydrogen evolution reaction, Chemical Engineering Journal 302 (2016) 437-445.
[25] S. Mishra, P.K. Maurya, A.K. Mishra, 2H–MoS2 nanoflowers based high energy density solid state supercapacitor, Materials Chemistry and Physics 255 (2020) 123551.
[26] I. Hussain, A. Ali, C. Lamiel, S.G. Mohamed, S. Sahoo, J.-J. Shim, A 3D walking palm-like core–shell $CoMoO_4$@ $NiCo_2S_4$@ nickel foam composite for high-performance supercapacitors, Dalton Transactions 48(12) (2019) 3853-3861.
[27] C. Wei, N. Zhan, J. Tao, S. Pang, L. Zhang, C. Cheng, D. Zhang, Synthesis of hierarchically porous NiCo2S4 core-shell hollow spheres via self-template route for high performance supercapacitors, Applied Surface Science 453 (2018) 288-296.

[28] Z. Hu, Z. Guo, Z. Zhang, M. Dou, F. Wang, Bimetal zeolitic imidazolite framework-derived iron-, cobalt-and nitrogen-codoped carbon nanopolyhedra electrocatalyst for efficient oxygen reduction, ACS applied materials & interfaces 10(15) (2018) 12651-12658.
[29] Z. Xiao, Y. Bao, Z. Li, X. Huai, M. Wang, P. Liu, L. Wang, Construction of Hollow Cobalt–Nickel Phosphate Nanocages through a Controllable Etching Strategy for High Supercapacitor Performances, ACS Applied Energy Materials 2(2) (2019) 1086-1092.
[30] T. Yoon, T. Bok, C. Kim, Y. Na, S. Park, K.S. Kim, Mesoporous silicon hollow nanocubes derived from metal–organic framework template for advanced lithium-ion battery anode, ACS nano 11(5) (2017) 4808-4815.
[31] R. Yang, X. Yan, Y. Li, X. Zhang, J. Chen, Nitrogen-doped porous carbon-ZnO nanopolyhedra derived from ZIF-8: new materials for photoelectrochemical biosensors, ACS applied materials & interfaces 9(49) (2017) 42482-42491.
[32] X. Han, K. Tao, D. Wang, L. Han, Design of a porous cobalt sulfide nanosheet array on Ni foam from zeolitic imidazolate frameworks as an advanced electrode for supercapacitors, Nanoscale 10(6) (2018) 2735-2741.
[33] Y. Ding, Y. Peng, S. Chen, Z. Li, X. Zhang, P. Falaras, L. Hu, A competitive coordination strategy to synthesize Co_3O_4@ carbon flower-like structures for high-performance asymmetric supercapacitors, Applied Surface Science 495 (2019) 143502.
[34] P. Zhang, B.Y. Guan, L. Yu, X.W. Lou, Formation of Double‐Shelled Zinc–Cobalt Sulfide Dodecahedral Cages from Bimetallic Zeolitic Imidazolate Frameworks for Hybrid Supercapacitors, Angewandte Chemie 129(25) (2017) 7247-7251.
[35] P. Cai, T. Liu, L. Zhang, B. Cheng, J. Yu, ZIF-67 derived nickel cobalt sulfide hollow cages for high-performance supercapacitors, Applied Surface Science 504 (2020) 144501.
[36] X. Lai, R. Guo, C. Cui, E. Ren, H. Xiao, Q. Qin, S. Jiang, Y. Zhang, Co-N codoped carbon/Co@ carbon cloth hybrid derived from ZIF-67 for oxygen evolution reaction and supercapacitor, Energy & Fuels (2020).
[37] Q. Wang, F. Gao, B. Xu, F. Cai, F. Zhan, F. Gao, Q. Wang, ZIF-67 derived amorphous $CoNi_2S_4$ nanocages with nanosheet arrays on the shell for a high-performance asymmetric supercapacitor, Chemical Engineering Journal 327 (2017) 387-396.
[38] S.-L. Jian, L.-Y. Hsiao, M.-H. Yeh, K.-C. Ho, Designing a carbon nanotubes-interconnected ZIF-derived cobalt sulfide hybrid nanocage for supercapacitors, Journal of Materials Chemistry A 7(4) (2019) 1479-1490.
[39] J.-L. Zhuang, X.-Y. Liu, H.-L. Mao, C. Wang, H. Cheng, Y. Zhang, X. Du, S.-B. Zhu, B. Ren, Hollow carbon polyhedra derived from room temperature synthesized iron-based metal-organic frameworks for supercapacitors, Journal of Power Sources 429 (2019) 9-16.
[40] X. Guan, M. Huang, L. Yang, G. Wang, X. Guan, Facial design and synthesis of CoSx/Ni-Co LDH nanocages with rhombic dodecahedral structure for high-performance asymmetric supercapacitors, Chemical Engineering Journal 372 (2019) 151-162.
[41] H. Chen, M.Q. Wang, Y. Yu, H. Liu, S.-Y. Lu, S.-J. Bao, M. Xu, Assembling hollow cobalt sulfide nanocages array on graphene-like manganese dioxide nanosheets for superior electrochemical capacitors, ACS applied materials & interfaces 9(40) (2017) 35040-35047.
[42] Y. Lu, L. Yu, M. Wu, Y. Wang, X.W. Lou, Construction of complex Co_3O_4@ Co_3V2O_8 hollow structures from metal–organic frameworks with enhanced lithium storage properties, Advanced Materials 30(1) (2018) 1702875.
[43] C. Xiao, Y. Xie, The expanding energy prospects of metal organic frameworks, Joule 1(1) (2017) 25-28.

[44] B.Y. Guan, L. Yu, X. Wang, S. Song, X.W. Lou, Formation of onion‐like NiCo2S4 particles via sequential ion‐exchange for hybrid supercapacitors, Advanced materials 29(6) (2017) 1605051.
[45] C. Hao, L. Wang, F. Wen, J. Xiang, L. Li, W. Hu, Z. Liu, Layer structured bismuth selenides Bi_2Se_3 and Bi_3Se_4 for high energy and flexible all-solid-state micro-supercapacitors, Nanotechnology 29(8) (2018) 085401.
[46] Z. Jiang, Z. Li, Z. Qin, H. Sun, X. Jiao, D. Chen, LDH nanocages synthesized with MOF templates and their high performance as supercapacitors, Nanoscale 5(23) (2013) 11770-11775.
[47] P. Li, Y. Yang, E. Shi, Q. Shen, Y. Shang, S. Wu, J. Wei, K. Wang, H. Zhu, Q. Yuan, Core-double-shell, carbon nanotube@ polypyrrole@ MnO_2 sponge as freestanding, compressible supercapacitor electrode, ACS applied materials & interfaces 6(7) (2014) 5228-5234.
[48] K. Li, S. Feng, C. Jing, Y. Chen, X. Liu, Y. Zhang, L. Zhou, Assembling a double shell on a diatomite skeleton ternary complex with conductive polypyrrole for the enhancement of supercapacitors, Chemical Communications 55(91) (2019) 13773-13776.
[49] Y. Fu, X. Gao, D. Zha, J. Zhu, X. Ouyang, X. Wang, Yolk–shell-structured MnO_2 microspheres with oxygen vacancies for high-performance supercapacitors, Journal of Materials Chemistry A 6(4) (2018) 1601-1611.
[50] X. Chang, L. Zang, S. Liu, M. Wang, H. Guo, C. Wang, Y. Wang, In situ construction of yolk–shell zinc cobaltite with uniform carbon doping for high performance asymmetric supercapacitors, Journal of Materials Chemistry A 6(19) (2018) 9109-9115.
[51] T. Dong, M. Li, P. Wang, P. Yang, Synthesis of hierarchical tube-like yolk-shell Co3O4@ NiMoO4 for enhanced supercapacitor performance, International Journal of Hydrogen Energy 43(31) (2018) 14569-14577.
[52] A.M. Zardkhoshoui, M.M. Ashtiani, M. Sarparast, S.S.H. Davarani, Enhanced the energy density of supercapacitors via rose-like nanoporous ZnGa2S4 hollow spheres cathode and yolk-shell FeP hollow spheres anode, Journal of Power Sources 450 (2020) 227691.
[53] K. Yang, Y. Yan, W. Chen, D. Zeng, C. Ma, Y. Han, W. Zhang, H. Kang, Y. Wen, Y. Yang, Yolk-shell bimetallic metal-organic frameworks derived multilayer core-shells $NiCo_2O_4$/NiO structure spheres for high-performance supercapacitor, Journal of Electroanalytical Chemistry 851 (2019) 113445.
[54] P. Xu, H. Liu, Q. Zeng, X. Li, Q. Li, K. Pei, Y. Zhang, X. Yu, J. Zhang, X. Qian, Yolk− Shell Nano ZnO@ Co‐Doped NiO with Efficient Polarization Adsorption and Catalysis Performance for Superior Lithium− Sulfur Batteries, Small 17(3) (2021) 2005227.
[55] Y. Guo, J. Tang, H. Qian, Z. Wang, Y. Yamauchi, One-pot synthesis of zeolitic imidazolate framework 67-derived hollow Co_3S_4@ MoS_2 heterostructures as efficient bifunctional catalysts, Chemistry of Materials 29(13) (2017) 5566-5573.
[56] W. Wang, Y. Lu, M. Zhao, R. Luo, Y. Yang, T. Peng, H. Yan, X. Liu, Y. Luo, Controllable tuning of cobalt nickel-layered double hydroxide arrays as multifunctional electrodes for flexible supercapattery device and oxygen evolution reaction, ACS nano 13(10) (2019) 12206-12218.
[57] X. Qian, W. Wu, J. Zhuang, Y. Niu, J. Huang, L. Hou, CoMoSx@ Ni-CoMoSx double-shelled cage-in-cage hollow polyhedron as enhanced Pt-free catalytic material for high-efficiency dye-sensitized solar cell, Journal of Power Sources 417 (2019) 21-28.
[58] T.S. Mathis, N. Kurra, X. Wang, D. Pinto, P. Simon, Y. Gogotsi, Energy storage data reporting in perspective—guidelines for interpreting the performance of electrochemical energy storage systems, Advanced Energy Materials 9(39) (2019) 1902007.

[59] X. Kong, B. Xia, Y. Xiao, H. Chen, H. Li, W. Chen, P. Wu, Y. Shen, J. Wu, S. Li, Regulation of cobalt–nickel LDHs' structure and components for optimizing the performance of an electrochemical sensor, ACS Applied Nano Materials 2(10) (2019) 6387-6396.
[60] R.R. Salunkhe, J. Tang, Y. Kamachi, T. Nakato, J.H. Kim, Y. Yamauchi, Asymmetric supercapacitors using 3D nanoporous carbon and cobalt oxide electrodes synthesized from a single metal–organic framework, ACS nano 9(6) (2015) 6288-6296.
[61] G. Yilmaz, K.M. Yam, C. Zhang, H.J. Fan, G.W. Ho, In situ transformation of MOFs into layered double hydroxide embedded metal sulfides for improved electrocatalytic and supercapacitive performance, Advanced Materials 29(26) (2017) 1606814.
[62] Z. Hu, Z. Zhang, Z. Li, M. Dou, F. Wang, One-step conversion from core–shell metal–organic framework materials to cobalt and nitrogen codoped carbon nanopolyhedra with hierarchically porous structure for highly efficient oxygen reduction, ACS applied materials & interfaces 9(19) (2017) 16109-16116.
[63] H. Zhu, Z. Li, F. Xu, Z. Qin, R. Sun, C. Wang, S. Lu, Y. Zhang, H. Fan, Ni3Se4@ CoSe2 hetero-nanocrystals encapsulated into CNT-porous carbon interpenetrating frameworks for high-performance sodium ion battery, Journal of Colloid and Interface Science (2021).
[64] N. Yanai, M. Sindoro, J. Yan, S. Granick, Electric field-induced assembly of monodisperse polyhedral metal–organic framework crystals, Journal of the American Chemical Society 135(1) (2013) 34-37.
[65] M. Ammar, S. Jiang, S. Ji, Heteropoly acid encapsulated into zeolite imidazolate framework (ZIF-67) cage as an efficient heterogeneous catalyst for Friedel–Crafts acylation, Journal of Solid State Chemistry 233 (2016) 303-310.
[66] Z. Sun, X.L. Wu, J. Xu, D. Qu, B. Zhao, Z. Gu, W. Li, H. Liang, L. Gao, Y. Fan, Construction of bimetallic selenides encapsulated in nitrogen/sulfur co‐doped hollow carbon nanospheres for high‐performance sodium/potassium‐ion half/full batteries, Small 16(19) (2020) 1907670.
[67] W. Zhong, Q. Ma, W. Tang, Y. Wu, W. Gao, Q. Yang, J. Yang, M. Xu, Construction of a bimetallic nickel–cobalt selenide pompon used as a superior anode material for high performance sodium storage, Inorganic Chemistry Frontiers 7(4) (2020) 1003-1011.
[68] Z. Ali, T. Tang, X. Huang, Y. Wang, M. Asif, Y. Hou, Cobalt selenide decorated carbon spheres for excellent cycling performance of sodium ion batteries, Energy Storage Materials 13 (2018) 19-28.
[69] T. Ma, M. Zhang, H. Liu, Y. Wang, Three-dimensional sulfur-doped graphene supported cobalt-molybdenum bimetallic sulfides nanocrystal with highly interfacial storage capability for supercapacitor electrodes, Electrochimica Acta 322 (2019) 134762.
[70] F. Ma, J. Lu, L. Pu, W. Wang, Y. Dai, Construction of hierarchical cobalt-molybdenum selenide hollow nanospheres architectures for high performance battery-supercapacitor hybrid devices, Journal of colloid and interface science 563 (2020) 435-446.
[71] S. Prabhakaran, J. Balamurugan, N.H. Kim, J.H. Lee, Hierarchical 3D oxygenated cobalt molybdenum selenide nanosheets as robust trifunctional catalyst for water splitting and zinc–air batteries, Small 16(19) (2020) 2000797.
[72] A.M. Zardkhoshoui, S.S.H. Davarani, Construction of complex copper-cobalt selenide hollow structures as an attractive battery-type electrode material for hybrid supercapacitors, Chemical Engineering Journal 402 (2020) 126241.
[73] C. Miao, C. Zhou, H.-E. Wang, K. Zhu, K. Ye, Q. Wang, J. Yan, D. Cao, N. Li, G. Wang, Hollow Co–Mo–Se nanosheet arrays derived from metal-organic framework for high-performance supercapacitors, Journal of Power Sources 490 (2021) 229532.

[74] H. Peng, G. Ma, K. Sun, Z. Zhang, J. Li, X. Zhou, Z. Lei, A novel aqueous asymmetric supercapacitor based on petal-like cobalt selenide nanosheets and nitrogen-doped porous carbon networks electrodes, Journal of Power Sources 297 (2015) 351-358.
[75] S.P. Vattikuti, K. Devarayapalli, P. Nagajyothi, J. Shim, Microwave synthesized dry leaf-like mesoporous $MoSe_2$ nanostructure as an efficient catalyst for enhanced hydrogen evolution and supercapacitor applications, Microchemical Journal 153 (2020) 104446.
[76] L.T. Le, D.Q. Truong, T.T. Ung, L.H. Nguyen, L.D. Vu, P.D. Tran, Cu2MoS4 Nanotubes as a Cathode Material for Rechargeable Magnesium‐ion Battery, ChemistrySelect 5(1) (2020) 280-283.
[77] T. Deepalakshmi, T.T. Nguyen, N.H. Kim, K.T. Chong, J.H. Lee, Rational design of ultrathin 2D tin nickel selenide nanosheets for high-performance flexible supercapacitors, Journal of Materials Chemistry A 7(42) (2019) 24462-24476.
[78] B. Kirubasankar, V. Murugadoss, J. Lin, T. Ding, M. Dong, H. Liu, J. Zhang, T. Li, N. Wang, Z. Guo, In situ grown nickel selenide on graphene nanohybrid electrodes for high energy density asymmetric supercapacitors, Nanoscale 10(43) (2018) 20414-20425.
[79] H. Peng, J. Zhou, K. Sun, G. Ma, Z. Zhang, E. Feng, Z. Lei, High-performance asymmetric supercapacitor designed with a novel NiSe@ $MoSe_2$ nanosheet array and nitrogen-doped carbon nanosheet, ACS Sustainable Chemistry & Engineering 5(7) (2017) 5951-5963.
[80] Y. Zhu, Z. Huang, Z. Hu, L. Xi, X. Ji, Y. Liu, 3D interconnected ultrathin cobalt selenide nanosheets as cathode materials for hybrid supercapacitors, Electrochimica Acta 269 (2018) 30-37.
[81] D. Chu, D. Guo, B. Xiao, L. Tan, H. Ma, H. Pang, X. Wang, Y. Jiang, 3D Hollow Flower‐like CoWO4 Derived from ZIF‐67 Grown on Ni‐foam for High‐Performance Asymmetrical Supercapacitors, Chemistry–An Asian Journal 15(11) (2020) 1750-1755.
[82] C.V.M. Gopi, H.-J. Kim, Design of Supercapacitor for Electric and Hybrid Vehicles: Supercapacitor, 2018 International Conference on Information and Communication Technology Robotics (ICT-ROBOT), IEEE, 2018, pp. 1-3.
[83] M.-X. Wang, J. Zhang, H.-L. Fan, B.-X. Liu, X.-B. Yi, J.-Q. Wang, ZIF-67 derived Co_3O 4/carbon aerogel composite for supercapacitor electrodes, New Journal of Chemistry 43(15) (2019) 5666-5669.
[84] Y. Li, L. Xu, M. Jia, L. Cui, J. Gao, X.-J. Jin, Hydrothermal Synthesis and Characterization of Litchi-Like $NiCo_2Se_4$@ carbon Microspheres for Asymmetric Supercapacitors with High Energy Density, Journal of The Electrochemical Society 165(9) (2018) E303.

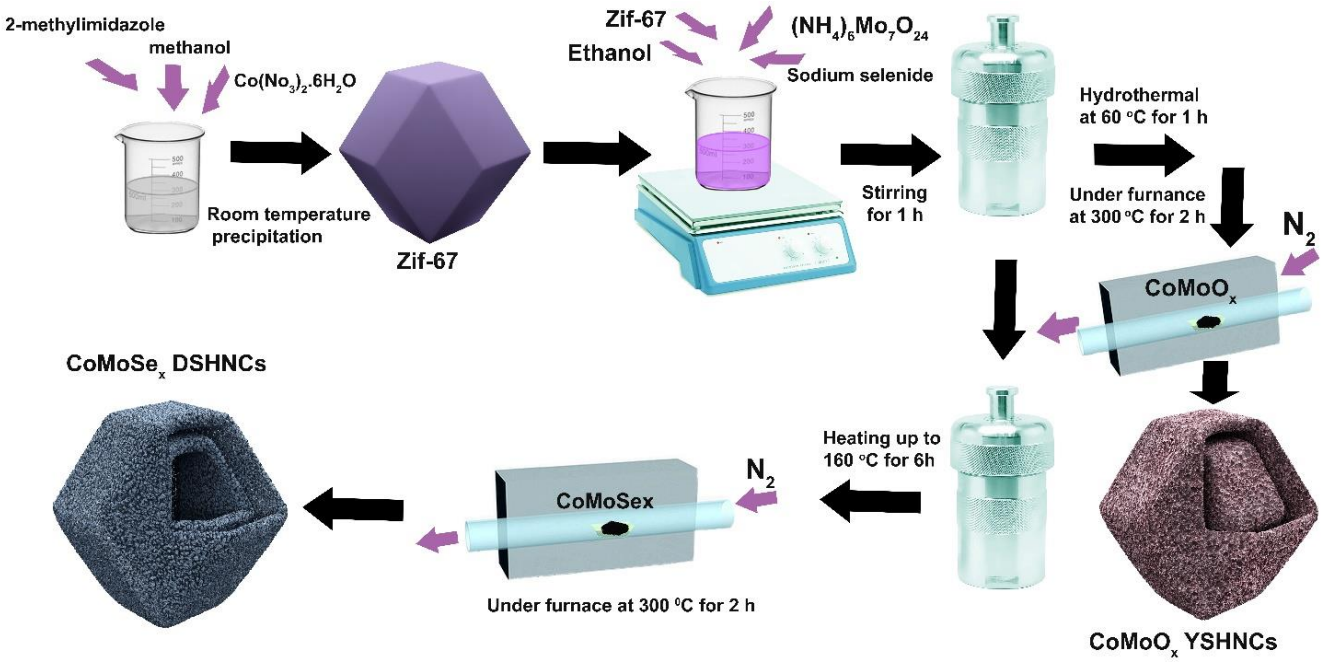

Figure 1: Schematic illustrations of structures and preparation process of CMS-DSHNCs.

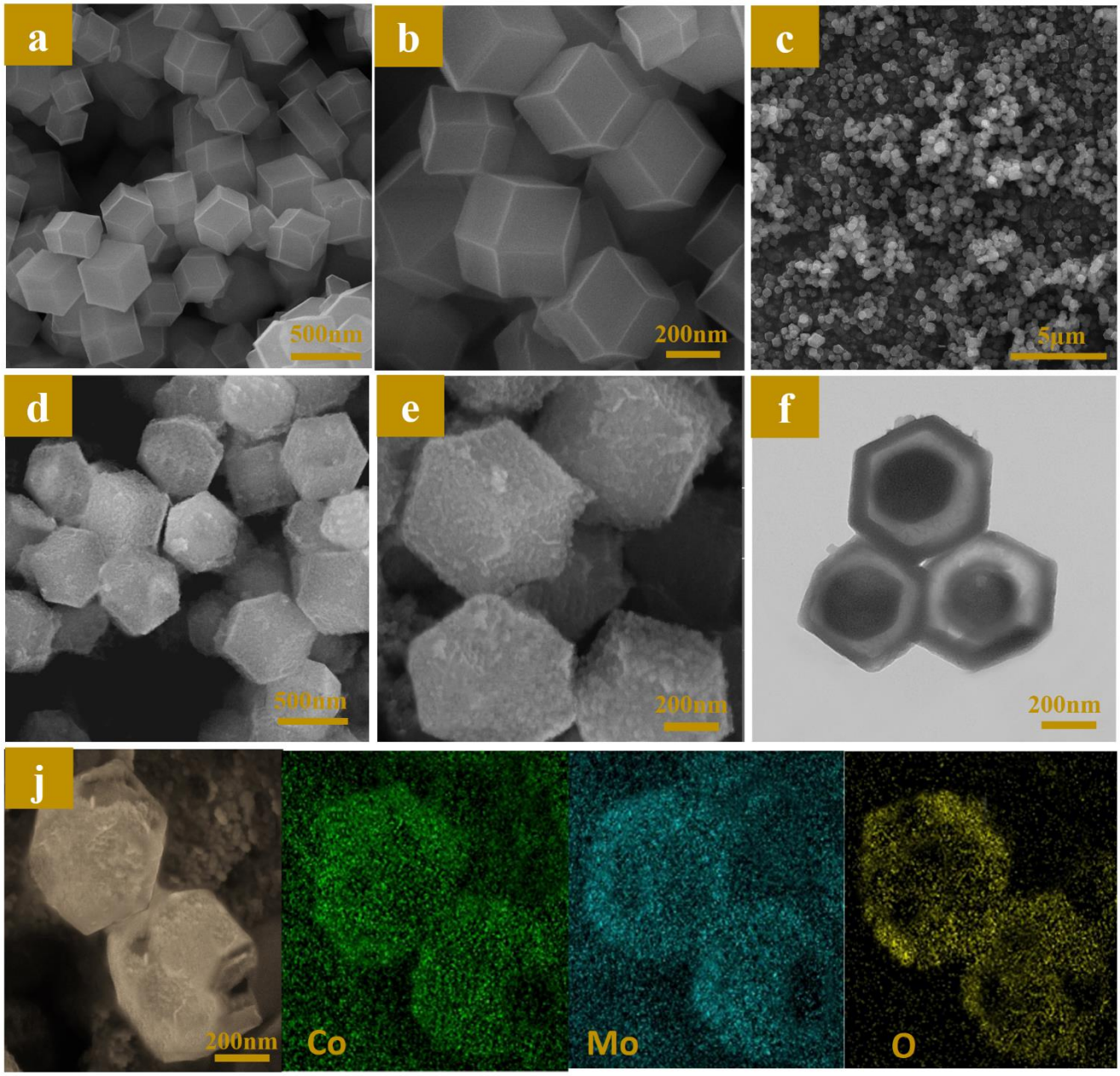

Figure 2: FESEM images of (a,b) ZIF-67 nanocages, (c-e) CMO-YSHNCs, (f) TEM images of the CMO-YSHNCs, and (j) SEM and the corresponding elemental mappings of CMO-YSHNCs.

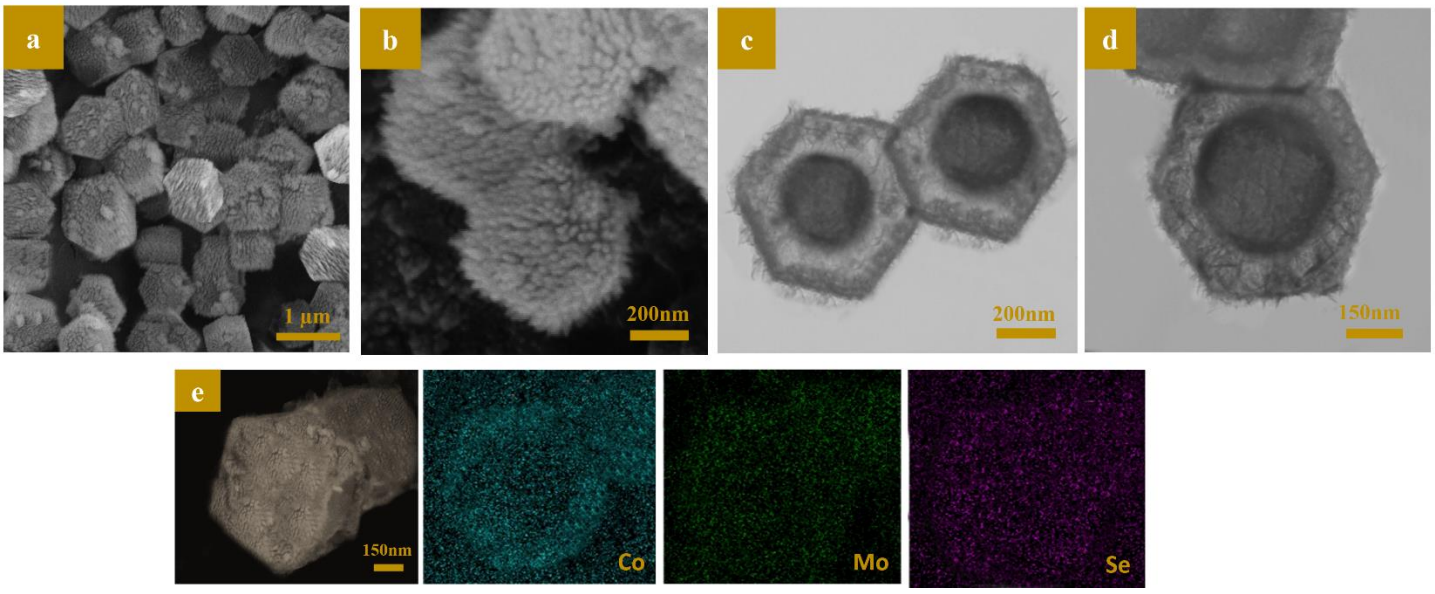

Figure 3: FESEM images of (a,b) the CMS-DSHNCs, (c-d) TEM images of the CMS-DSHNCs, and (e) SEM and corresponding elemental mappings of the CMS-DSHNCs.

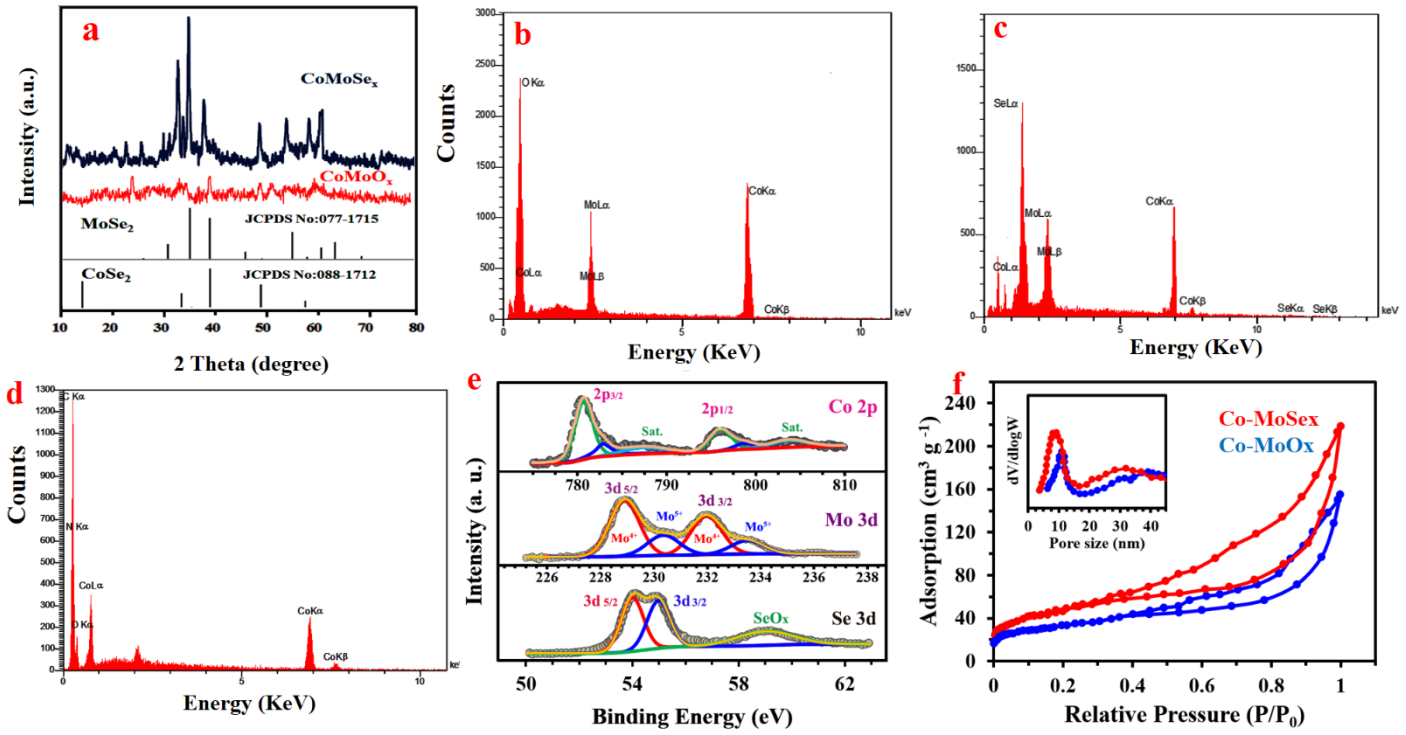

Figure 4: (a) XRD patterns of the CMO-YSHNCs and CMS-DSHNCs, (b) EDX spectrum of the CMO-YSHNCs, (c) EDX spectrum of the CMS-DSHNCs, and (d) EDX spectrum of the Zif-67. (e) XPS spectra of Co 2p and Mo 2p, and Se 2p of the CMS-DSHNCs sample, (f) N_2 adsorption–desorption isotherms of the CMO-YSHNCs and CMS-DSHNCs samples, and its corresponding BJH pore size distribution curves (inset).

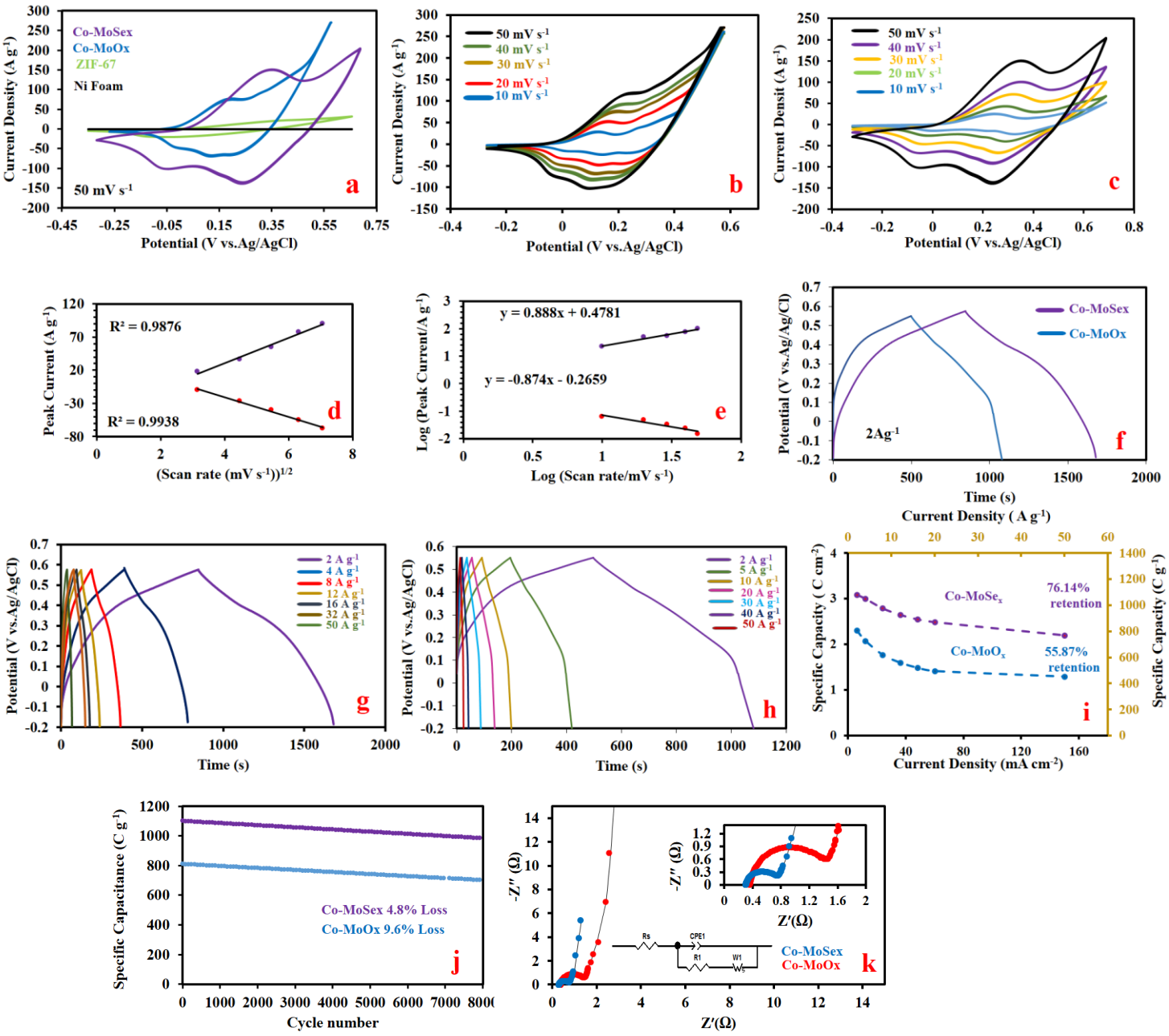

Figure 5. Electrochemical characterizations of as-prepared the CMS-DSHNCs electrode in a three-electrode system. (a) CV of the Ni foam, ZIF-67 nanocages, CMO-YSHNCs, and CMS-DSHNCs electrodes at a scan rate of 50 mV s^{-1} in aqueous 3.0 M KOH electrolyte. (b) CV curves of the CMO-YSHNCs electrode at various scan rates in aqueous 3.0 M KOH electrolyte. (c) CV curves of CMS-DSHNCs electrode at various scan rates in aqueous 3.0 M KOH electrolyte. (d) Linear plot of anodic/ cathodic peak current as a function of the square root of scan rate. (e)Linear plot of logarithm of peak current as a function of the logarithm of scan rate. (f) GCD plots of the CMO-YSHNCs and CMS-DSHNCs electrodes at 2 A g^{-1}. (g) GCD plots of

the CMS-DSHNCs electrode at various current densities. (h) GCD plots of the Co-MoO_x YSHNCs electrode at various current densities. (i) Rate capability of the CMO-YSHNCs and CMS-DSHNCs electrodes. (j) The durability of the CMO-YSHNCs and CMS-DSHNCs electrodes at a current density of 8 mA cm^{-2}.(k) Nyquist plots of the CMO-YSHNCs and CMS-DSHNCs electrodes.

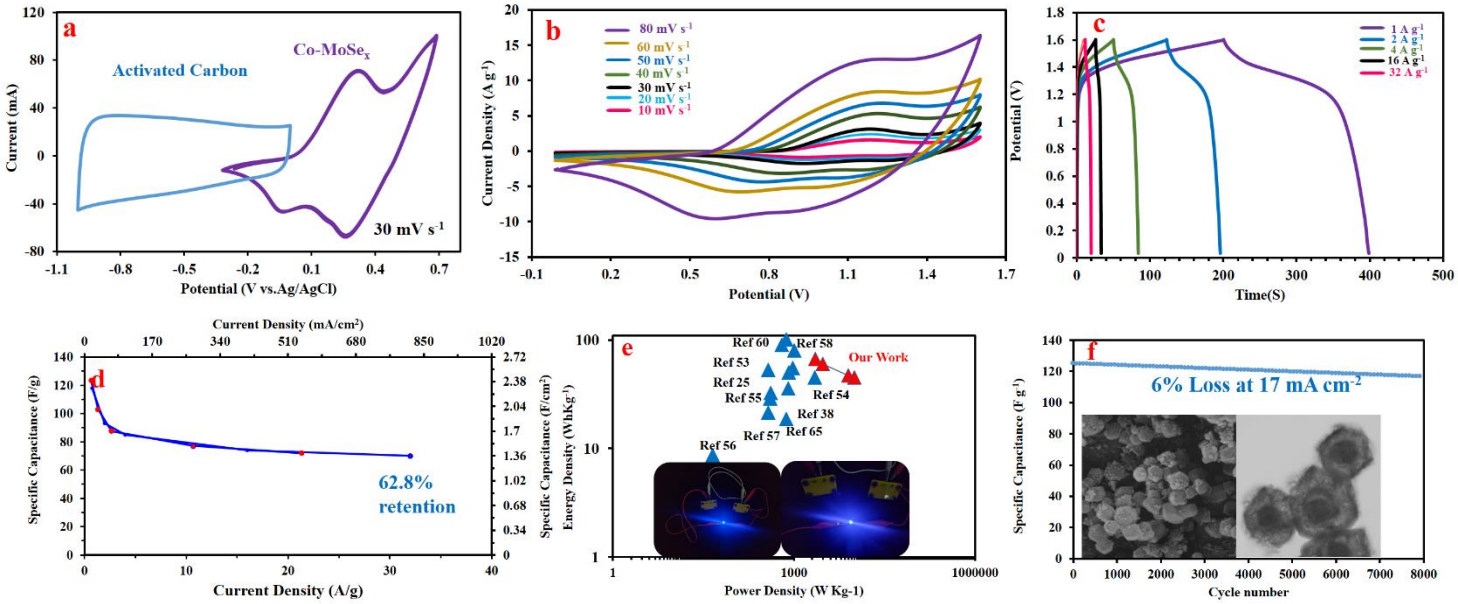

Figure 6: Electrochemical characterizations of CMS-DSHNCs (+)//AC (-) asymmetric supercapacitors. (a) CV curves of AC and CMS-DSHNCs electrodes at a scan rate of 30 mV s^{-1} in a half-cell system. (b) CVs of the prepared CMS-DSHNCs (+)//AC (-) asymmetric device at different scan rates. (c) GCD plots of the asymmetric device at different current densities. (d) Rate capability of the device. (e) Comparison between Ragone plot of CMS-DSHNCs (+)//AC (-) device with previously reported devices (the inset depicts the real application of two devices in series that can light up the red LED). (f) The durability of the device after 8000 CD cycles at a high current density of 17 mA cm^{-2}.

Material	Three-electrode system		Synthesis route	Two- electrode system				Refs.
	Specific capacitance at current density	Cycle retention		Specific capacitance at current density	Cycle retention	E Max (W h Kg^{-1})	P (W Kg^{-1})	
$Sn_{0.33}Ni_{0.67}Se_2$/nanosheets	346 mA h g^{-1}, 1.0 mA cm^{-2}	99.6%,10000	Hydrothermal	112.6 mAhg^{-1}, at 2.0 mA cm^{-2}	96.41%, 10000	90.3	631	[77]
NiSe–G/nanohybrids	1280 F g^{-1}, 1 Ag^{-1}	98%, 2500	Hydrothermal	141 Fg^{-1}, at 1 Ag^{-1}	84.4%, 3000	50.1	816	[78]
NiSe@$MoSe_2$/nanosheet	223 F g^{-1}, 1 Ag^{-1}	80%, 5000	Hydrothermal	71.5 Fg^{-1}, at 1 Ag^{-1}	91.4%, 5000	32.6	415	[79]
CoSe/nanosheets	70.6 mAh g^{-1} at 1 A g^{-1}	52.8%, 20000	Hydrothermal	-	95.4%, 20000	18.6	750	[80]
$CoWO_4$ Derived ZIF-67 / Hollow Flower-like	1395 F g^{-1}, .5 Ag^{-1}	89.00%, 3000	Hydrothermal	81 F g^{-1} , at 1 Ag^{-1}	89.00%, 3000	29.0	404	[81]
$CoNiSe_2$/microspheres	183.4 mA h g^{-1}, 1 Ag^{-1}	99.2%, 3000	Hydrothermal	577.4 F g^{-1}, at 1 Ag^{-1}	97.02%, 3000	80.2	1000	[82]
ZIF-67 derived Co_3O_4 /carbon aerogel/nanosheets	298.8 F g^{-1},at 0.5 A g^{-1}	82%, 1000	Hydrothermal	-	-	-	-	[83]
NiCo2S4/hollow sphere	1870.2 F g^{-1},at 2.0 A g−1	91%, 3000	Hydrothermal	169.4 F g^{-1}, at 0.5 A g^{-1}	95.9% ,3000	52.9	374	[27]
NiCo2Se4@carbon Microspheres	1394 F g^{-1}, at .5 A g^{-1}	80%,10000	Hydrothermal	721F g^{-1},at 0.5 A g^{-1}	81%,10000	101	749	[84]
CoS_x/Ni-Co LDH /nanocages	1562 F g^{-1}, at 1 A g^{-1}	85.18%, 5000	Reflux condition	-	94.56%, 10000	35.8	800	[40]
Co-MoSex/DSHNCs	1029.8 C g^{-1},at 2 A g^{-1}	95.2%, 8000	Hydrothermal	125F g^{-1},at 1 A g^{-1}	94%, 8000	45	2222	This work